Technical Notes

Fuel-Optimal Formation Reconfiguration by Means of Unidirectional Low-Thrust Propulsion System

Ahmed Mahfouz*
University of Luxembourg, 1855 Luxembourg, Luxembourg
Gabriella Gaias†
Politecnico di Milano, 20156 Milan, Italy
Florio Dalla Vedova‡
LuxSpace, 6832 Betzdorf, Luxembourg
and
Holger Voos§
University of Luxembourg, 1855 Luxembourg, Luxembourg

https://doi.org/10.2514/1.G008214

I. Introduction

LOW-THRUST electric propulsion systems are becoming the preferred design solution for small-class and CubeSat-based satellite platforms [1]. This is motivated by many factors, among which is the fact that they are generally more fuel efficient than their chemical counterparts. Furthermore, electric thrusters require significantly less propellant mass, which leads to lighter launch mass and consequently reduces the costs [2]. To further minimize the complexity of the system design and/or to meet stringent power/mass constraints of small satellite platforms, the propulsion system typically features a single throttleable electric thruster. Examples of such satellites include Triton-X Medium and Heavy [3], the PLATiNO platform [4], and the Gravity Field and Steady-State Ocean Circulation Explorer satellite [5]. Small satellites are often incorporated in multisatellite missions to build disaggregated instruments and to carry out inspection tasks. These demand the capability to perform formation reconfiguration by means of unidirectional electric propulsion systems. In this Note, the term *unidirectional* signifies that the propulsion system comprises a single un-gimbaled thruster.

While the problem of relative orbit reconfiguration has been widely addressed, most existing approaches are tailored for satellites equipped with impulsive thrusters [6–9], which are not suitable for low-thrust electric propulsion. Some guidance schemes have been proposed for low-thrust systems, such as those developed for the Formation Flying L-band Aperture Synthesis mission [10] and for collision avoidance maneuver optimization [11]. However, these schemes often assume omnidirectional thrusting capability, limiting their applicability to unidirectional systems. In contrast, the Autonomous Vision Approach Navigation and Target Identification (AVANTI) mission [12] adopted a unidirectional impulsive propulsion system. The guidance algorithm used in AVANTI, which is only suited for impulsive thrust, allowed the reorientation of the thruster nozzle through planned control windows [7,13]. Furthermore, model predictive control (MPC) schemes were proposed in Refs. [14,15] to address the problem of formation reconfiguration and formation keeping for satellites which are equipped with single electric thrusters. However, these approaches do not account for critical mission operational constraints, such as necessary thruster-off periods due to operational considerations. Additionally, they rely on more complex formulations compared to the simpler and more efficient approach proposed in this Note.

In this Note, the problem of autonomous optimal formation reconfiguration is addressed for a formation which comprises two satellites, a chief and a deputy, where only the deputy has orbit maneuvering capabilities through a single throttleable electric thruster. The Note comes as part of the AuFoSat toolbox to support the future formation flying missions of Triton-X, a multimission microsatellite platform developed by LuxSpace to accommodate various types of payloads in low Earth orbits (LEOs). Previous AuFoSat research discussed orbit design [16], relative navigation [17,18], and absolute orbit keeping for Triton-X [15]. While the developed algorithms in the framework of AuFoSat are meant to primarily be used onboard Triton-X, the goal is to provide a guidance, navigation, and control toolbox that could be used by any satellite with the same, or similar, specifications as Triton-X.

In the context of unidirectional relative orbit reconfiguration, an attitude slew maneuver is necessary before each thruster firing so that the nozzle could be aligned with the required thrust direction before the firing takes place. The problem is approached through formulating a trajectory optimization (guidance) problem as a fuel-optimal constrained convex optimization problem with multiple no-thrust windows during which attitude redirection slews takes place. This, in turn, requires constant alternation between the on and off states of the thruster. One big advantage of this on–off alternation is the ability to accommodate long no-thrust periods which arise from mission constraints, for example, eclipse, during which electric thrusters are usually turned off because the solar arrays are not generating electricity. The biggest advantage of the proposed guidance scheme is that, by relaxing some of the original constraints, it can be transformed into a quadratic programming (QP) problem which can be solved efficiently using any of the standard QP solvers. This makes it an attractive candidate to be implemented onboard a satellite that uses one of the commercial-off-the-shelf onboard computers. The control loop is then closed through a shrinking-horizon MPC scheme where the optimization of the state and input thrust profiles (from the current to the final time) are optimized using the proposed guidance algorithm. It should be noted that the control logic does not necessitate the guidance algorithm to be run at each MPC step but rather uses the previous guidance profile if the current state is close, within a predefined threshold, to its value predicted by the previous guidance solution.

The main contributions of this Note are 1) an efficient guidance scheme for formation reconfiguration with a single electric thruster, 2) the ability to accommodate multiple long-duration no-thrust periods, and 3) an MPC algorithm that optimizes state and input thrust profiles without requiring frequent guidance recalculations.

This Note presents applications where collision avoidance is not of a concern for the satellite reconfigurations. Nonetheless, if required by a specific application, the proposed methodology is straightforwardly applicable by adding the collision avoidance constraints

Received 17 January 2024; accepted for publication 9 September 2024; published online Open Access 5 December 2024.

*Doctoral Researcher, Interdisciplinary Centre for Security, Reliability and Trust (SnT), 29 Avenue J.F. Kennedy; Ahmed.mahfouz@uni.lu (Corresponding Author).

†Associate Professor, Department of Aerospace Science and Technology, 34 via La Masa.

‡Senior Engineer, 9 Rue Pierre Werner.

§Full Professor, Interdisciplinary Centre for Security, Reliability and Trust (SnT) and Faculty of Science, Technology and Medicine, 6 Rue Richard Coudenhove-Kalergi, 1359 Luxembourg, Luxembourg, 29 Avenue J.F. Kennedy.

through the relaxed formulation generally adopted in the literature [19]. By including such relaxed constraints, in fact, the overall optimization problem is still cast into the QP formulation, thus featuring all the proposed advantages. Note that in the remainder of the text, the terms *fuel-optimal* and ΔV*-optimal* are used interchangeably. These two terms are identical only in the case of single-directional propulsion systems [20].

II. Dynamical Model

The reference frames used in this work are the Earth-centered-inertial frame, denoted as $\mathbb{F}^i$; the satellite-body-fixed frame, denoted as $\mathbb{F}^b$; and the radial–transversal–normal frame (RTN), denoted as $\mathbb{F}^r$. The reader is advised to refer to Ref. [15] for a full definition of these reference frames. Vectors expressed in $\mathbb{F}^i$, $\mathbb{F}^b$, or $\mathbb{F}^r$ are signified by the superscripts i, b, or r respectively.

The orbital motion of a satellite under the gravitational influence of a major body (e.g., the Earth) can be parameterized in a planet-centered inertial frame by the set of orbital elements

$$\boldsymbol{\alpha} \coloneqq \begin{bmatrix} a & u & e_x & e_y & i & \Omega \end{bmatrix}^\intercal \tag{1}$$

where a is the semimajor axis, u is the mean argument of latitude, $\boldsymbol{e} \coloneqq [\, e_x \quad e_y \,]^\intercal = [\, e\cos\omega \quad e\sin\omega \,]^\intercal$ is the eccentricity vector with e being the orbital eccentricity, i is the orbital inclination, and Ω is the right ascension of the ascending node. It is important to note that the motion of the satellite can also be parameterized by the Cartesian state vector, $\boldsymbol{x}^i \coloneqq [\, (\boldsymbol{r}^i)^\intercal \quad (\boldsymbol{v}^i)^\intercal \,]^\intercal$, where $\boldsymbol{r}^i$ and $\boldsymbol{v}^i$ are the absolute position and velocity vectors expressed in $\mathbb{F}^i$ which can be mapped to/from the orbital elements through a set of nonlinear equations [21]. The exact position and velocity of the spacecraft transform into osculating orbital elements, which in the remainder of this work will be denoted by $\tilde{\boldsymbol{\alpha}}$. Mean orbital elements, denoted by $\boldsymbol{\alpha}$, are to be intended as one-orbit averaged elements, where the short- and long-term oscillations generated by the J_2 harmonic of the Earth gravitational potential are removed. Mean/osculating elements' conversions are performed through the transformations developed in Ref. [22].

The relative motion between a deputy and a chief spacecraft can be described by the dimensionless quasi-nonsingular relative orbital elements (ROE) vector, which is a nonlinear transformation of the orbital elements vector introduced in Eq. (1),

$$\begin{aligned} \delta\boldsymbol{\alpha} &\coloneqq \begin{bmatrix} \delta a & \delta\lambda & \delta e_x & \delta e_y & \delta i_x & \delta i_y \end{bmatrix}^\intercal \\ &= \begin{bmatrix} \Delta a/a_c & \Delta u + \Delta\Omega\cos i_c & \Delta e_x & \Delta e_y & \Delta i & \Delta\Omega\sin i_c \end{bmatrix}^\intercal \end{aligned} \tag{2}$$

where $\delta\boldsymbol{\alpha}$ is the dimensionless ROE vector, δa is the relative semimajor axis, $\delta\lambda$ is the relative mean longitude, $\delta\boldsymbol{e} \coloneqq [\, \delta e_x \quad \delta e_y \,]^\intercal$ is the relative eccentricity vector, and $\delta\boldsymbol{i} \coloneqq [\, \delta i_x \quad \delta i_y \,]^\intercal$ is the relative inclination vector. It is to be noted that here, and in the coming discussions, the subscript d denotes a quantity related to the deputy satellite, while the subscript c is used for chief-related quantities. Moreover, $\delta(\cdot)$ signifies a relative quantity between the deputy and the chief which is not necessarily the arithmetic difference between that of the deputy and that of the chief, while $\Delta(\cdot)$ signifies the arithmetic difference between $(\cdot)_d$ and $(\cdot)_c$, that is, $\Delta(\cdot) \coloneqq (\cdot)_d - (\cdot)_c$. As in the case of absolute orbital elements, the osculating ROE vector is denoted by $\delta\tilde{\boldsymbol{\alpha}}$, whereas the mean ROE vector is referred to as $\delta\boldsymbol{\alpha}$. A dimensional ROE vector is obtained by multiplying the dimensionless ROE vector by the semimajor axis of the chief,

$$\boldsymbol{y} \coloneqq a_c\delta\boldsymbol{\alpha} \tag{3}$$

where $\boldsymbol{y}$ is the dimensional mean ROE vector with units of length.

Assuming neighboring orbits of the chief and the deputy, and a near-circular orbit of the chief, the dynamics of the ROE can be linearized to the first order considering the mean effect of the J_2 zonal harmonic. In fact, a closed-form solution of the linearized dynamics can be obtained for piecewise constant input acceleration as discussed in Ref. [8]. The system evolution is expressed in the form

$$\boldsymbol{y}(t_{k+1}) = \boldsymbol{\Phi}(t_k, t_{k+1})\boldsymbol{y}(t_k) + \frac{a_c}{M}\boldsymbol{\Psi}(t_k, t_{k+1})\boldsymbol{f}^r(t_k, t_{k+1}) \tag{4}$$

where $\boldsymbol{\Phi}(t_k, t_{k+1})$ is the state transition matrix between the two time instants t_k and t_{k+1}, $\boldsymbol{\Psi}(t_k, t_{k+1})$ is the convolution matrix between the same two time instants, M is the deputy's mass which is assumed constant throughout any maneuver, and $\boldsymbol{f}^r(t_k, t_{k+1}) = [\, f_R \quad f_T \quad f_N \,]^\intercal$ is the input thrust vector in $\mathbb{F}^r$, constant over the period $[t_k, t_{k+1}]$. In the rest of the text, and in order to simplify the representation of equations, the following notations are used: $\boldsymbol{\Phi}_{k|k+1} \equiv \boldsymbol{\Phi}(t_k, t_{k+1})$, $\boldsymbol{\Psi}_{k|k+1} \equiv \boldsymbol{\Psi}(t_k, t_{k+1})$, $\boldsymbol{y}_k \equiv \boldsymbol{y}(t_k)$, and $\boldsymbol{f}^r_{k|k+1} \equiv \boldsymbol{f}^r(t_k, t_{k+1})$.

III. Guidance

In this section, a multiple shooting guidance scheme is developed when large relative orbit maneuvers are required between two satellites, a deputy and a chief, where the chief might be either a physical satellite or a virtual one. The deputy satellite is assumed to be equipped with a single throttleable electric thruster, which not only mandates redirection slew maneuvers before every thruster firing but also dictates the thruster to operate perpetually because it provides low thrust. It is for these reasons that the guidance scheme is designed from the beginning to operate on an alternating on–off mode where the throttleable thruster is turned off to allow the attitude maneuver to take place. The trajectory optimization problem is formulated such that a change in relative orbit is required from $\boldsymbol{y}_0$ at t_0 to a reference $\boldsymbol{y}_f$ at t_f through $(m+1)/2$ continuous thruster firings, where m is an odd number. Figure 1 illustrates the alternation between thrust and attitude maneuvers throughout the allocated maneuver time, from t_0 to t_f. To enhance the predictability of the mission, the vector of time instants at which the thruster is turned on and off, $\boldsymbol{t} = [\, t_0 \quad t_1 \quad \ldots \quad t_f \,]$, is not treated as optimization variables and is left as a user input. In Fig. 1, $\forall l \in \mathcal{L} = \{1, 2, \ldots, (m+1)/2\}$, $T_{f,l}$ are the forced (thrust-powered) time periods, and $T_{n,l}$ are those during which the natural unforced translational dynamics take over (coast arcs).

A. Problem Formulation

Letting

$$\boldsymbol{Y} \coloneqq \begin{bmatrix} \boldsymbol{y}_0 & \boldsymbol{y}_1 & \cdots & \boldsymbol{y}_{m+1} \end{bmatrix}, \quad \boldsymbol{F} \coloneqq \frac{a_c}{M}\begin{bmatrix} \boldsymbol{f}^r_{0|1} & \boldsymbol{f}^r_{1|2} & \cdots & \boldsymbol{f}^r_{m|m+1} \end{bmatrix} \tag{5}$$

the guidance problem can be formally written as an optimization problem as follows.

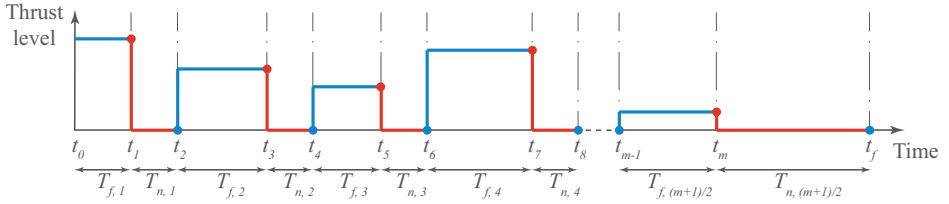

Fig. 1 Graphical representation of the low-thrust guidance scheme.

Problem 1:

$$\min_{\boldsymbol{Y},\boldsymbol{F}} \ \mathrm{tr}(\boldsymbol{F}^{\intercal}\boldsymbol{F}) \quad \text{subject to}$$

$$\boldsymbol{y}_0 = \boldsymbol{y}_0, \quad \boldsymbol{y}_{m+1} = \boldsymbol{y}_f, \quad \boldsymbol{y}_{k+1} = \boldsymbol{\Phi}_{k|k+1}\boldsymbol{y}_k + \frac{a_c}{M}\boldsymbol{\Psi}_{k|k+1}\boldsymbol{f}^r_{k|k+1} \quad \forall\, k \in \mathcal{K} \tag{6}$$

$$\boldsymbol{f}^r_{k|k+1} = \boldsymbol{0} \quad \forall\, k \in \mathcal{K}_n \tag{7}$$

$$\left\|\boldsymbol{f}^r_{k|k+1}\right\| \le f_{\max} \quad \forall\, k \in \mathcal{K}_f \tag{8}$$

Here, $\mathcal{K} = \mathcal{K}_f \cup \mathcal{K}_n$, with $\mathcal{K}_f = \{0, 2, 4, \ldots, m-1\}$ and $\mathcal{K}_n = \{1, 3, 5 \ldots, m\}$. It can be inferred that the $\mathcal{K}$ is the set of indices of all time steps used in the trajectory optimization scheme, $\mathcal{K}_f$ is the set of indices of all time instances at which the thruster is turned on, and $\mathcal{K}_n$ includes indices to the time instances at which the thruster is turned off (refer to Fig. 1). Moreover, $\mathrm{tr}(\cdot)$ is the matrix trace, and $f_{\max}$ is the maximum allowable thrust by the onboard thruster. Note that Eq. (7) is a hard constraint to assure there is no input thrust provided during attitude redirection maneuvers. Indeed, Problem 1 stands as a convex optimization problem (COP) because it fulfills all the necessary conditions for a problem to be one [23], which, namely, are as follows:

1) A cost function must be convex (for minimization problems).
2) Inequality constraints must be convex.
3) Equality constraints must be affine.

Being a COP, Problem 1 is guaranteed to have a globally optimal solution; however, it would be much more efficient to solve if it could be put in one of the standard classes of convex optimization problems, for example, linear programming, quadratic programming, and so on, because dedicated solvers for these classes have matured over the past decades. It is clear that the only thing which prevents Problem 1 from being put in the convex QP canonical form is constraint (8) because it is a quadratic constraint and not an affine one. It can be, nonetheless, transformed into multiple affine constraints using the methodology proposed in Ref. [24], which suggests that

$$\|\boldsymbol{b}\| \le d, \quad \boldsymbol{b} \in \mathbb{R}^2 \qquad \text{can be relaxed by}$$
$$\begin{bmatrix} \cos(\gamma_j) & \sin(\gamma_j) \end{bmatrix}\boldsymbol{b} \le d\cos(\gamma_{\max}) \quad \forall\, j \in \mathcal{J} \tag{9}$$

where $\mathcal{J} = \{1, 2, \ldots, n_{\mathrm{dir}}\}$, with $n_{\mathrm{dir}} \ge 3$ being the number of affine inequality constraints that approximate the Euclidean norm constraint; $\gamma_j = (2(j-1)\pi/n_{\mathrm{dir}}) + \gamma_{\mathrm{first}}$, with γ_{first} being the angle corresponding to the first direction; and $\gamma_{\max} = \pi/n_{\mathrm{dir}}$. It is important to emphasise that the constraint relaxation, Eq. (9), is only applicable to two-element vectors, while the norm constraint in Problem 1, constraint (8), is imposed on a three-element vector $\boldsymbol{f}^r_{k|k+1}$. The relaxation is, therefore, applied the projection of the constraining sphere on each plane individually. The ROE dynamics (refer to Ref. [8]) possess unique characteristics that necessitates an accurate approximation of the constraining circle lying in the Transversal-Normal plane, while coarse approximations of the constraints on the two other planes are acceptable. Concretely, the optimal solution to Problem 1 is expected to rarely incorporate radial thrust [7,14] because it is known to be more expensive, from the ΔV point of view, than relying solely on transversal thrust, especially when the reconfiguration can afford long maneuver times for large in-plane maneuvers. It is for this reason that the relaxation in Eq. (9) is applied in the T-N plane with a larger number of directions n_{dir} than the number of directions used in the Radial-Transversal and the Radial-Normal planes. Namely, we introduce $\bar{n}_{\mathrm{dir}} = 4 < n_{\mathrm{dir}}$ as the number of directions that approximates the constraining circles lying in the R-T and the R-N planes, with $\bar{\gamma}_j = (2(j-1)\pi/\bar{n}_{\mathrm{dir}}) + \bar{\gamma}_{\mathrm{first}} \forall j \in \bar{\mathcal{J}} = \{1, \ldots, \bar{n}_{\mathrm{dir}}\}$ and with $\bar{\gamma}_{\max} = \bar{\gamma}_{\mathrm{first}} = \pi/4$. In this setting, the constraints in the R-T and the R-N planes are approximated by two rhombuses which cover only around 64% of the original constraining circles.

Having introduced the constraint relaxations which transform a quadratic constraint into multiple affine ones, the reformulation of Problem 1 as a QP problem can be written as follows.

Problem 2:

$$\min_{\boldsymbol{Y},\boldsymbol{F}} \ \mathrm{tr}(\boldsymbol{F}^{\intercal}\boldsymbol{F}) \quad \text{subject to}$$

$$\boldsymbol{y}_0 = \boldsymbol{y}_0, \quad \boldsymbol{y}_{m+1} = \boldsymbol{y}_f, \quad \boldsymbol{y}_{k+1} = \boldsymbol{\Phi}_{k|k+1}\boldsymbol{y}_k + \frac{a_c}{M}\boldsymbol{\Psi}_{k|k+1}\boldsymbol{f}^r_{k|k+1} \quad \forall\, k \in \mathcal{K} \tag{10}$$

$$\boldsymbol{f}^r_{k|k+1} = \boldsymbol{0} \quad \forall\, k \in \mathcal{K}_n \tag{11}$$

$$\begin{bmatrix} 0 & \cos(\gamma_j) & \sin(\gamma_j) \end{bmatrix}\boldsymbol{f}^r_{k|k+1} \le f_{\max}\cos(\gamma_{\max}), \quad \forall\, j \in \mathcal{J} \,\&\, \forall\, k \in \mathcal{K}_f \tag{12}$$

$$\begin{bmatrix} \cos(\bar{\gamma}_j) & \sin(\bar{\gamma}_j) & 0 \\ \cos(\bar{\gamma}_j) & 0 & \sin(\bar{\gamma}_j) \end{bmatrix}\boldsymbol{f}^r_{k|k+1} \le f_{\max}\cos(\bar{\gamma}_{\max}), \quad \forall\, j \in \bar{\mathcal{J}} \,\&\, \forall\, k \in \mathcal{K}_f \tag{13}$$

A graphical representation of the feasibility regions of the control thrust components is given in Fig. 2 for both problems, Problem 1 and Problem 2. In Fig. 2, the constraint relaxation in Eq. (9) is depicted for $n_{\mathrm{dir}} = 10$ and $\gamma_{\mathrm{first}} = 0$, which covers approximately 94% of the original constraining circle in the T-N plane.

It is important to note that, while the relaxed constraint (13) does not explicitly constrain the radial thrust component any better than the original circular constraint, it does, however, affect the choice of the radial–transversal and normal–radial combinations.

B. Parameters Sensitivity Analysis

Investigating the two proposed formulations of the guidance Problems 1 and 2 and their graphical representation Fig. 1, it can be deduced that the parameters that are provided by the user and might need tuning are, namely the time instances at which the thruster is switched on and off (or alternatively the time periods $T_{f,l}$ and $T_{n,l} \forall l \in \mathcal{L}$ as well as the allocated maneuver time, $t_f - t_0$). The choice of the time periods $T_{f,l}$ and $T_{n,l}$ is generally subject to mission time constraints, for example, not being able to provide thrust during eclipse, during ground contact, or during scientific experiments. If no such mission constraints are present, fixing the time periods $T_{f,l}$ and $T_{n,l}$ comes as a natural choice, that is, $T_{f,l} = T_f$, $T_{n,l} = T_n \forall l \in \mathcal{L}$. For this specific case, a sensitivity analysis is performed to assess the feasibility of the optimization problem when the values of T_f and T_n change. In this sensitivity analysis, Problem 2 was solved for 100

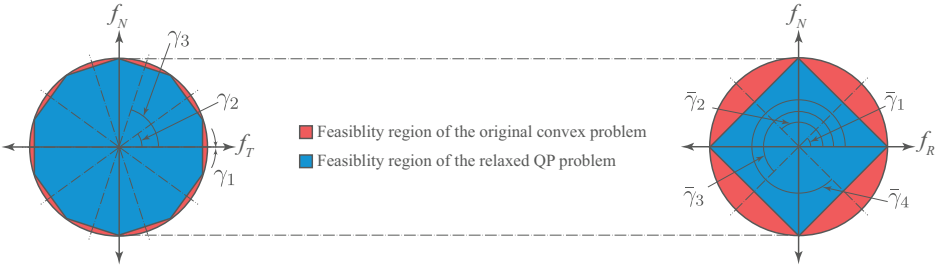

Fig. 2 Feasibility region comparison between the original COP (Problem 1) and the QP problem (Problem 2).

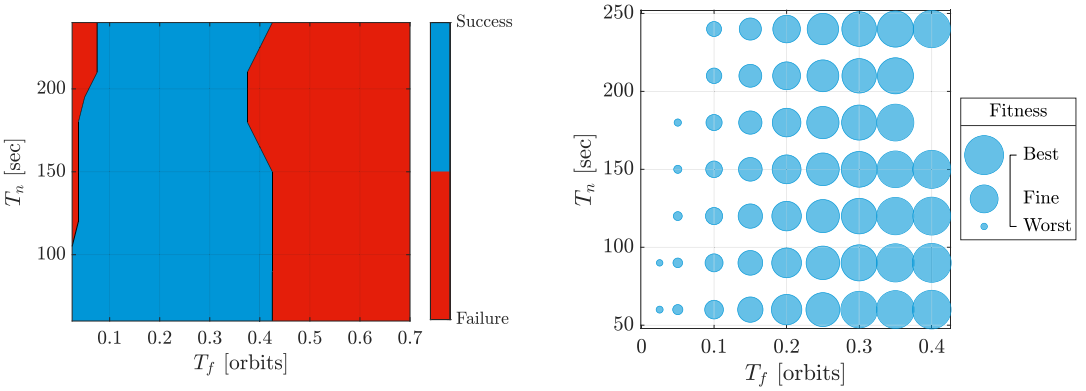

a) Optimization success region under varying T_f and T_n **b) Fitness within the success region**

Fig. 3 Sensitivity of the system to T_f and T_n variations.

randomly chosen initial conditions, that is, $\boldsymbol{y}_0$, for the 91 T_f-T_n combination drawn from $T_n \in \{60, 90, \ldots, 240\}$ s and $T_f \in \{0.025, 0.05, 0.1, \ldots, 0.5, 0.6, 0.7\}$ orbits. Furthermore, because the difference between the initial and the final ROE vectors is what characterizes the maneuver, and not the values of the vectors themselves, only the value of $\boldsymbol{y}_0$ is chosen randomly, while the value of $\boldsymbol{y}_f$ is set to zero for the 9100 experiments. Namely, the entries of the initial dimensional ROE vector $\boldsymbol{y}_0$ are chosen randomly from the $[-1\ 1]$ km range, except for the initial relative mean argument of longitude $a\delta\lambda_0$, which is chosen randomly from the $[-100\ \ 100]$ km. The allocated time for the maneuver is fixed to 15 orbits, the osculating orbital elements of the chief at the beginning of the maneuver were fixed to $\tilde{\boldsymbol{\alpha}}_{c,0} = [7121\text{ km}\ 0°\ 10^{-3}\ 0\ 85°\ 0°]^\intercal$, and the number of directions that approximate the maximum thrust constraint in the T-N plane is fixed to $n_{\text{dir}} = 12$.

The output of the sensitivity analysis is the success and failure regions in the T_f-T_n plane, where the success region is that in which the optimizer succeeded to find a feasible solution for all the 100 random initial conditions. The success and failure regions of the aforementioned sensitivity study are depicted in Fig. 3a.

Indeed, not all the points within the success region are the same from the fuel-efficiency point of view, because changing T_f and T_n does, in turn, change the cost function. A fitness function is introduced to assess the competence of each T_f-T_n combination within the success region. The adopted fitness function is the reciprocal of the average optimal cost over the 100 initial conditions at each T_f-T_n point. The fitness is calculated at each point in the success region, and the results are presented in Fig. 3b. It is clear from Fig. 3b that changing the value of T_n barely changes the fitness for a fixed T_f value, while it is obvious that the larger the value of T_f, the fitter the T_f-T_n combination. Nevertheless, there comes a point where increasing T_f drives the combination out of the success region (see Fig. 3a). It is for this reason that the adopted value of T_f in many of the numerical experiments to follow is set to 0.3, which is a value that guarantees acceptable fitness and is, at the same time, far away from the failure region.

Although the purpose of the sensitivity analysis is ultimately to help choose adroit values for T_f and T_n, because the time necessary for a slew maneuver heavily depends on the maximum slew rate $\omega_{\max}$ for any specific satellite, the value of T_n can be calculated analytically according to the following formula:

$$T_n = \frac{\pi}{\omega_{\max}} + T_{\text{safety}} \tag{14}$$

The rationale behind Eq. (14) is that, because the maximum possible slew angle is π, the longest time period it takes the satellite to perform any slew, using the maximum angular speed, is $\pi/\omega_{\max}$. Indeed, the satellite never uses the maximum angular speed throughout the whole slew, which is why the T_{safety} term is added to make sure that the allocated time for the slew maneuver T_n is always more than enough. The importance of T_{safety} is not limited to insuring the coast arc is sufficient for the slew maneuver; it also proves to be useful in closing the loop as will be discussed in Sec. V. For Triton-X, the maximum slew rate is 2 deg/s, and hence T_n is calculated to be 100 s after choosing $T_{\text{safety}} = 10$ s.

IV. Guidance Scheme Validation

After comparing the performance of many different convex QP solvers, the free open-source Operator Splitting Quadratic Program (OSQP) [25] stood as the fastest and was hence chosen to solve Problem 2 in the coming discussions. To validate the proposed guidance scheme for the targeted maneuver spectrum, the optimization problem is solved for a variety of maneuvers, large and otherwise, using the parameters chosen based on the sensitivity study, and the results of one of these tests is reported here. In that experiment, the initial and final dimensional ROE vectors are randomly chosen to be $\boldsymbol{y}_0 = [-55.6\ 7414.7\ \ -58.7\ 83.7\ \ -2.3\ 22.4]^\intercal$ m and $\boldsymbol{y}_f = \boldsymbol{0}$, while the initial orbit of the chief is defined in terms of the osculating orbital elements such that $\tilde{\boldsymbol{\alpha}}_{c,0} = [7121\text{ km}\ 0°\ 10^{-5}\ 0\ 45°\ 0°]^\intercal$. The full parameters list of the reported maneuver is presented in Table 1. Note that choosing $\boldsymbol{y}_f$ to be zeros means that the two satellites are required to rendezvous at the final time. It is to be noted that the satellite mass, the maximum thrust, and the maximum slew rate are extracted from the publicly available Triton-X specifications.[¶] Moreover, n_{dir} is set to 12 as this is the least number of directions that approximates the constraining circle by multiple affine constraints while covering at least 95% of the its area.

In Fig. 4, the dimensional ROE profile, optimized by the guidance scheme, is depicted. The plots in Fig. 4 reveal that the main goal of the guidance algorithm, which is to rendezvous with the virtual chief at the final time, is achieved. Moreover, the $\delta\lambda$ error is corrected through building δa momentum according to the natural dynamics of the ROE [8], instead of firing in the radial direction.

The level of thrust provided by the onboard electric propulsion system is presented in Fig. 5a. It is clear that the maximum thrust constraint is respected thanks to the relaxations (12) and (13) that approximate the original quadratic constraint (8). Furthermore, the fact

Table 1 Parameters used in the guidance scheme validation simulation

Parameter	Value	Parameter	Value
$t_f - t_0$, orbits	5	T_f, orbits	0.3
T_n, s	100	n_{dir}	12
γ_{first}, °	0	M, kg	200
$f_{\max}$, mN	7	$\omega_{\max}$, °/s	2

[¶]The Triton-X brochure can be found at https://www.ohb.de/fileadmin/artundweise/downloads/Triton-

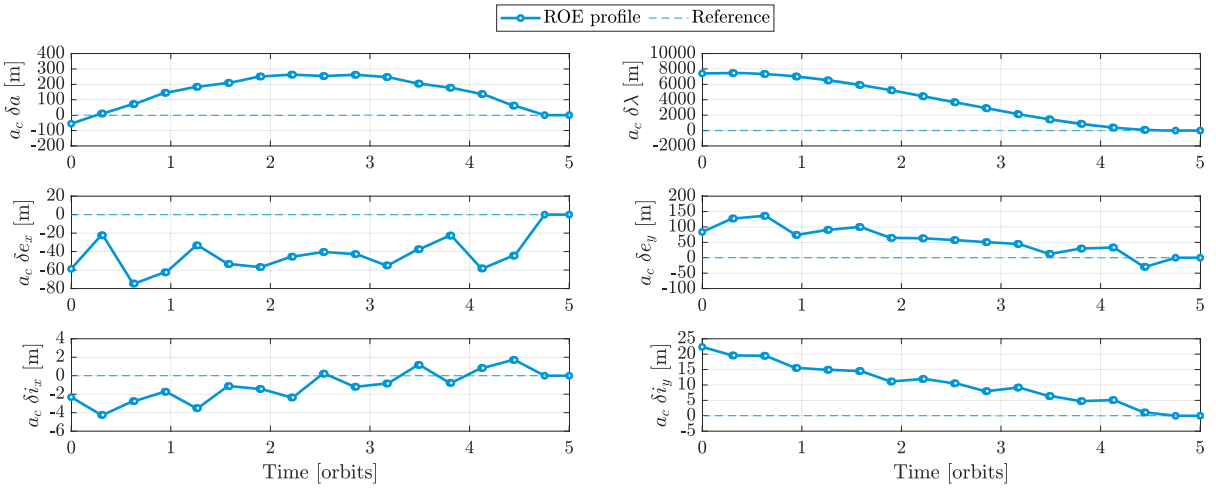

Fig. 4 Optimized dimensional ROE profile.

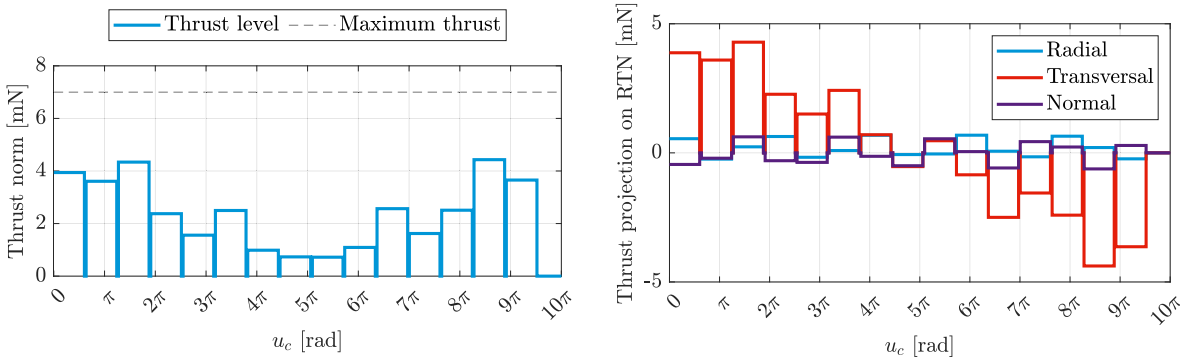

a) Thrust norm **b) Thrust projection into the RTN frame**

Fig. 5 Optimized thrust profile.

that the satellite uses minimal radial thrust, as expected, is evident in Fig. 5b, which depicts the projection of the thrust into the RTN frame.

When Problem 1 was solved, for the guidance validation simulation, using a solver called "Mosek", the resulting solution was nearly identical to that of Problem 2. The two solutions are so similar that they are almost indistinguishable. The primary difference lies in the total required ΔV. Specifically, Problem 1 required slightly less ΔV (0.3296 m/s) compared to Problem 2, which required 0.3297 m/s, accounting for only a 0.03% increase in ΔV for Problem 2. However, this minor reduction in ΔV for Problem 1 comes at the cost of a significantly longer solve time. The mean solve time of Problem 1, using Mosek, was 15.05 ms, which is substantially longer than the 0.65 ms mean solve time required by Problem 2 when solved using OSQP. These solve times represent the average over 10 runs for each problem.

Satellite missions usually have constraints on the timing of the orbital maneuvers, which arise from not being able to perform any thruster firing, for example, during ground contact or during eclipse periods. Unlike impulsive-thrust absolute/relative orbit correction maneuvers, low-thrust maneuvers may take too long to execute, days in some cases. It is for this reason that low-thrust guidance algorithms need to accommodate the no-thrust periods during the orbital maneuver itself. One of the main contributions of this Note is the ability of the proposed guidance scheme to adapt to different scenarios where the thruster is required to shut down for known extended periods without the need to change the structure of the problem. The duration of each coast arc $T_{n,l}$ (see Fig. 1), which is a user input, is the only thing that needs to be adapted according to the operational constraints. To evaluate the capability of the trajectory optimization routine to handle long coast arcs, two scenarios

X_Heavy_Specification_and_Description_2021.pdf [retrieved 21 November 2024].

Table 2 Adopted no-thrust periods for two simulation scenarios

Scenario	No-thrust periods, orbits
Scenario 1	{0.5–1, 1.5–2, 2.5–3, 3.5–4, 4.5–5}
Scenario 2	{0.25–0.5, 1.25–2.25, 3–3.25, 4.25–4.75}

are considered. In both scenarios, the maneuver duration and the initial and final ROE vectors remain fixed, while only the no-thrust periods are varied. The thruster-off periods are arbitrarily chosen for each of the two scenarios and are reported in Table 2. The initial and final dimensional ROE vectors for both scenarios are set to $\boldsymbol{y}_0 = [187\,945\;189\;86\;79\;-114]^\intercal$ m and $\boldsymbol{y}_f = [0412\;389\;-96\;153\;-198]^\intercal$ m, and the simulation parameters are identical to those reported in Table 1 except for T_f, which is set to 0.1 orbits. This reduction of the value of T_f is motivated by the fact that, given the large durations of the coast arcs, the problem would become infeasible if T_f is kept 0.3. One other way to overcome infeasibility would be to increase the maneuver time.

The user-defined no-thrust intervals for the two defined scenarios can be seen graphically in Fig. 6, in which the expected behavior of the thruster is presented. It is important to emphasize that, while the no-thrust periods are seen to appear with a regular pattern (from the halfway point to the end of each orbit) for scenario 1, this need not be the case for operational time constraints, which is reflected in scenario 2.

The dimensional ROE profile, predicted by the guidance algorithm, is depicted in Fig. 7 for both scenarios, where the thruster-off periods are also shown. It is obvious that the $\delta\lambda$ signal is conceivably evolving even when no thrust is provided because it can be manipulated not only directly through input thrust but also indirectly

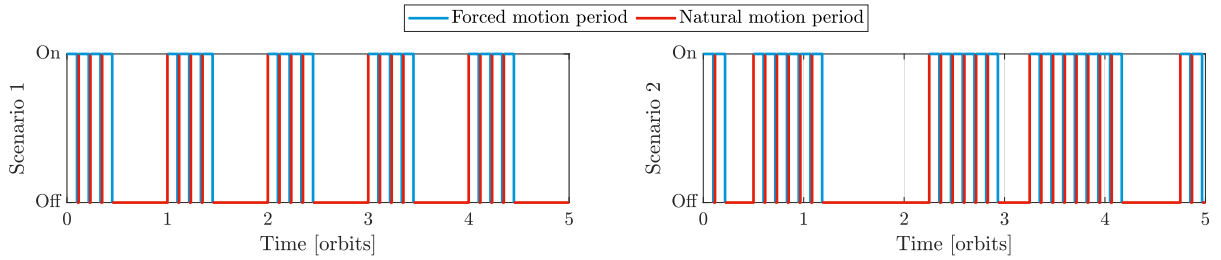

Fig. 6 Expected behavior of the thruster in the presence of the thruster-off periods in Table 2.

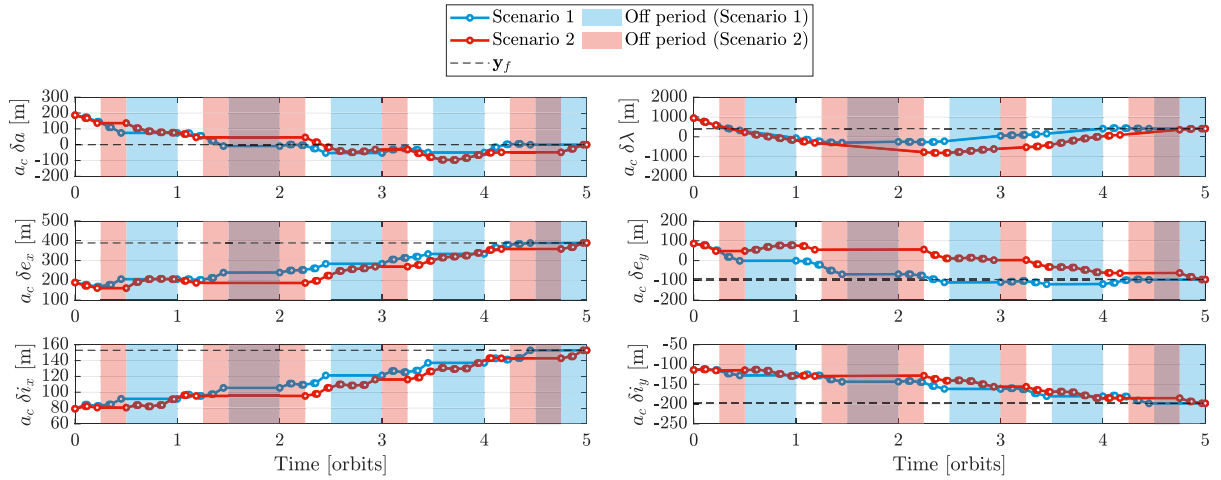

Fig. 7 Guidance dimensional ROE profile under operational constraints.

through the nonzero value of δa. Notably, the total Delta-V is different for each of the scenarios, as it counts to 0.286 m/s in the first scenario and to 0.303 m/s in the second.

V. Closing Loop

The proposed trajectory optimization scheme is an open-loop control system that does not consider disturbances or model inaccuracies. It is for this reason that the loop has to be closed to react to system changes in real time. In this section, the feedback control loop is studied, and the exact location of the guidance module within the closed loop is discussed. The simulated module execution logic onboard the deputy is depicted in Fig. 8, in which the solid arrows signify the main signals that are recurrently passed and the dashed lines are those which are passed only once before the beginning of the maneuver. In Fig. 8, the effect of Earth's oblateness on the osculating position and velocity vectors was the only external perturbation that was incorporated by the orbit propagators. Moreover, Osc2Mean is the function that transforms osculating orbital elements to mean ones [22], and RTN2Inertial is the method that rotates any vector from $\mathbb{F}^r$ to $\mathbb{F}^i$ given the position and velocity of the chief (or alternatively its orbital elements) at the time instant in question. Moreover, the breve accent $\breve{}$ signifies a quantity which is disturbed by either one or a combination of 1) estimation errors, for example, $\breve{\boldsymbol{\alpha}}_{d,k}$; b) Attitude Determination and Control System (ADCS) inaccuracies, for example, $\breve{\boldsymbol{f}}^i_{k|k+1}$; or c) physical constraints of the actuators, for example, $\breve{\boldsymbol{f}}^i_{k|k+1}$. Note that in quantities with double subscripts the first subscript refers to the spacecraft, either chief or deputy, and the second refers to the time instant at which the quantity is evaluated; for example, $\breve{\boldsymbol{\alpha}}_{d,k}$ is the perturbed mean orbital elements vector of the deputy at time t_k.

Because the navigation module is out of the scope of this Note, and in order to take the hardware inaccuracies and physical limitations into account within the numerical simulations, surrogate models for

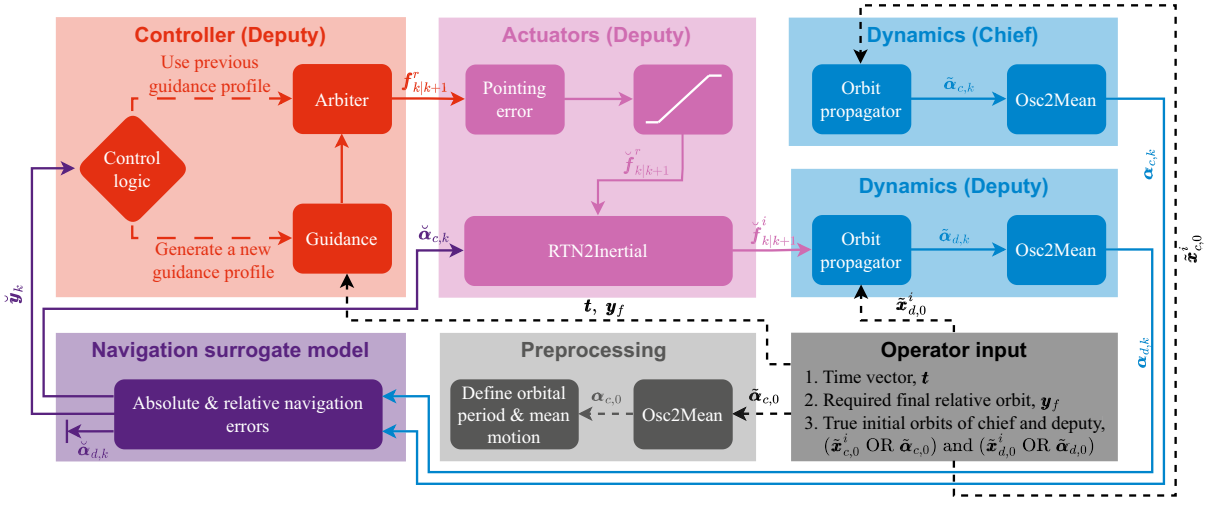

Fig. 8 Deputy's module execution logic used in numerical simulations.

estimation inaccuracies as well as for the physical limitations and ADCS errors are introduced. The physical limitations are only present in the saturation block in Fig. 8, which can be easily implemented in the numerical simulations. In fact, this saturation is taken into account in the guidance implementation as the maximum thrust constraint [see constraints (12) and (13) of Problem 2]; nonetheless, it is also implemented in the control loop as a safeguard. The navigation surrogate model uses the input mean orbital elements of the deputy and the chief as ground truth. The following procedure is used on the chief spacecraft,

$$\begin{aligned} &\boldsymbol{x}^i_{c,k} = \text{OE2Cart}(\boldsymbol{\alpha}_{c,k}), \quad \check{\boldsymbol{x}}^i_{c,k} = \boldsymbol{x}^i_{c,k} + \mathcal{N}(\boldsymbol{0}, \boldsymbol{\Sigma}_{\boldsymbol{x}_c}), \\ &\check{\boldsymbol{\alpha}}_{c,k} = \text{Cart2OE}(\check{\boldsymbol{x}}^i_{c,k}) \end{aligned} \tag{15}$$

where the two methods OE2Cart and Cart2OE are those which transform the orbital elements vector into Cartesian state vector and vice versa [21], and $\mathcal{N}(\mu, \sigma^2)$ is a normally distributed random variable with μ as its mean and σ^2 as its variance. Hence, $\boldsymbol{\Sigma}_{\boldsymbol{x}_c}$ is the covariance matrix of the random noise affecting the estimation of the Cartesian state of the chief satellite, which is defined as

$$\boldsymbol{\Sigma}_{\boldsymbol{x}_c} = \text{diag}\left(\sigma^2_{\boldsymbol{r}_c}, \sigma^2_{\boldsymbol{r}_c}, \sigma^2_{\boldsymbol{r}_c}, \sigma^2_{\boldsymbol{v}_c}, \sigma^2_{\boldsymbol{v}_c}, \sigma^2_{\boldsymbol{v}_c}\right) \tag{16}$$

where $\text{diag}(\cdot, \cdot, \dots)$ is a function that creates a diagonal matrix, with zero off-diagonal elements, from its input arguments, and $\sigma^2_{\boldsymbol{r}_c}$ and $\sigma^2_{\boldsymbol{v}_c}$ are the variances of the one-dimensional (in the x, the y, or the z directions) position and velocity estimation errors, respectively. It is worth mentioning that the mean orbital elements of the deputy can be disturbed using the same model in Eq. (15), however, using different variances for the one-dimensional position and velocity estimation errors, namely, $\sigma_{\boldsymbol{r}_d}$ and $\sigma_{\boldsymbol{v}_d}$. Moreover, relative navigation is, in general, more accurate than the absolute one [18,26]. Hence, the surrogate model for the relative navigation needed to be more than just converting the estimated absolute orbital elements of the chief and the target to a ROE vector. The following surrogate model is used instead,

$$\delta\boldsymbol{\alpha} = \text{OE2ROE}(\boldsymbol{\alpha}_c(t), \boldsymbol{\alpha}_d), \qquad \check{\boldsymbol{y}} = a_c\delta\boldsymbol{\alpha} + \mathcal{N}(\boldsymbol{0}, \boldsymbol{\Sigma}_{\boldsymbol{y}}) \tag{17}$$

where OE2ROE is the method that transforms the orbital elements of the chief and deputy to a ROE vector according to Eq. (2) and $\boldsymbol{\Sigma}_{\boldsymbol{y}}$ is the covariance matrix of the zero mean normally distributed random disturbance vector, which can be expressed as

$$\boldsymbol{\Sigma}_{\boldsymbol{y}} = \text{diag}\left(\sigma^2_{\boldsymbol{y}}, \sigma^2_{\boldsymbol{y}}, \sigma^2_{\boldsymbol{y}}, \sigma^2_{\boldsymbol{y}}, \sigma^2_{\boldsymbol{y}}, \sigma^2_{\boldsymbol{y}}\right) \tag{18}$$

Lastly, the *Pointing error* block in Fig. 8 is using the the following surrogate model,

$$\mathfrak{q}_{\text{pe}} = \begin{bmatrix} \cos(\zeta_{\text{pe}}/2) & \sin(\zeta_{\text{pe}}/2)\hat{\boldsymbol{q}}^{\intercal}_{\text{pe}} \end{bmatrix}^{\intercal}, \quad \check{\boldsymbol{f}}^r_{k|k+1} = \mathfrak{q}_{\text{pe}} \circ \boldsymbol{f}^r_{k|k+1} \circ \tilde{\mathfrak{q}}_{\text{pe}} \tag{19}$$

where $\mathfrak{q}_{\text{pe}}$ is the thruster misalignment unit quaternion, with $\tilde{\mathfrak{q}}_{\text{pe}}$ being its quaternion conjugate; ζ_{pe} is the pointing error angle, which can be extracted from Triton-X brochure; $\hat{\boldsymbol{q}}_{\text{pe}}$ is a random three-element unit vector; and $\circ$ is the quaternion multiplication operator.

The *Controller* block collection in Fig. 8 works as a MPC where the prediction horizon spans from the current time to the user-defined maneuver end time, and the control and prediction horizons are identical. In this setting, the control profile optimization as well as the state prediction from the current time to the maneuver final time is done recurrently by the trajectory optimization scheme (Problem 2), and the function of the *Arbiter* block is only to choose the proper input thrust from the provided guidance profile, namely, the first or the second thrust vector from the guidance control profile depending on whether the current time lies within a forced or a natural translational motion period. The logic of the closed loop which is used in the validation simulations is elaborated upon in Algorithm 1. In this algorithm, $\boldsymbol{t}$ is the user-defined time vector for the guidance (see Fig. 1), $\boldsymbol{y}_f$ is the required final dimensional ROE vector, and ϵ is a tunable threshold.

The first guidance profile is conceivably calculated before the maneuver starting time t_0. As suggested by Algorithm 1, the trajectory might need to be optimized during the execution of the maneuver, and this is exactly when the importance of including T_{safety} within T_n becomes apparent. While T_{safety} guarantees that T_n is sufficient for the most stringent attitude redirection maneuver as Eq. (14) suggests, it is also used to optimize the next guidance profile if one needs to be optimized, for example, before t_2 or t_4 (see Fig. 1), which is very valuable from the practical point of view.

To test the performance of the closed-loop system using the proposed guidance scheme, it has been benchmarked against the MPC proposed in Ref. [14]. The out-of-plane (OOP) maneuver in Ref. [14] is chosen for this benchmark experiment because such maneuvers can give a clear insight about the fuel optimality (equivalent to ΔV optimality for unidirectional propulsion systems) of the control algorithm because only thrust in the normal direction is required. In fact, the exact locations (in terms of u_c) in which impulsive thrust should be provided for a ΔV-optimal OOP maneuver can be calculated analytically [7], which makes it easy for a human eye to recognize ΔV-optimal thrust profiles. For the low-thrust case, the thrust in the normal direction is expected to be distributed evenly around these locations for the control profile to be close to ΔV optimality, while the thrust components in the radial and transversal directions are expected to be around zero. The initial and final dimensional ROE vectors for benchmark maneuver as well as the chief's initial orbit are drawn from Ref. [14] to be $\boldsymbol{y}_0 = [0\ 0\ 273\ 0\ 10\ 70]^{\intercal}$ m, $\boldsymbol{y}_f = [0\ 0\ 273\ 0\ 400\ 120]^{\intercal}$ m, and $\tilde{\boldsymbol{\alpha}}_{c,0} = [6828\ \text{km}\ 0^\circ\ 10^{-5}\ 0\ 78^\circ\ 0^\circ]^{\intercal}$. A summary of the parameters used in the benchmark maneuver is provided in Table 3. All the parameters that are not reported are identical to the ones in Table 1 except for the length of the forced translational motion periods, which is set to $T_f = 0.3$ orbits for the first six orbits of the maneuver and to $T_f = 0.1$ orbits for the final orbit to allow for a more precise approach to the target relative orbit. It is important to note that, while $t_f - t_0, T_f, T_n$, and ϵ are tunable parameters, the values of $\sigma_{\boldsymbol{r}_d}$, $\sigma_{\boldsymbol{v}_d}$, and ζ_{pe} are extracted from the specification sheets of Triton-X even if the benchmark maneuver is assuming a different satellite.

The dimensional ROE profile generated by the proposed closed-loop system as well as that which is generated by the reference control scheme (the one proposed in Ref. [14]) are depicted in Fig. 9. It is clear that the two control algorithms could achieve the final required dimensional ROE vector $\boldsymbol{y}_f$ at the end of the maneuver at approximately the same time.

A comparison of the thrust profiles, projected to the RTN frame, between the proposed and the reference controllers is presented in Fig. 10. Because the maneuver is an OOP one, only thrust in the normal direction is expected to be exerted; however, one can notice that the reference control algorithm does occasionally fire in the transversal direction. The proposed as well as the reference controllers can be seen to provide almost no thrust in the radial direction. While this happens in the reference controller because a hard constraint is imposed on the radial thrust to be exactly zero, the proposed approach does not use radial thrust simply because it is optimal to not use it, as expected for this type of simulation scenarios. Furthermore, in Fig. 10, the two controllers are shown to distribute the available thrust around the ΔV-optimal locations because they are both ΔV-optimal algorithms.

Two key performance metrics are compared for both controllers, the proposed and the reference, in Table 4. The tables suggests that, although the proposed algorithm uses more total ΔV, ΔV_{tot}, than the reference one, the terminal error of the proposed controller is much less than that of the reference. Although the state prediction over the prediction horizon needs to be done recurrently, the guidance does not need to be run at each optimization step (see Fig. 8). It is evident in Algorithm 1 that the guidance is run only when the distance (in the dimensional ROE space) between current state and its prediction by the previous guidance profile is more than the threshold ϵ. To show how often the guidance problem needs to be solved over the benchmark simulation, the elapsed time for every guidance run is depicted in Fig. 11, in which an elapsed time of exactly zero means

Algorithm 1: Simulated Control Loop

Input: $\boldsymbol{t}$, $\boldsymbol{y}_f$, ϵ, $\tilde{\boldsymbol{\alpha}}_{c,0}$, $\tilde{\boldsymbol{\alpha}}_{d,0}$
for $k = 0 \to m$, **do**
  t_k, $t_{k+1} \leftarrow$ Elements with indices $k \to (k+1)$ in $\boldsymbol{t}$; // Identifying current and next time steps
  NoUpdateFlag $\leftarrow$ false; // A flag indicated whether the guidance profiles need to be updated or not
  if $k = 0$, **then** // Initial time step of the maneuver
    // At the initial step, a guidance profile needs to be calculated, the current horizon is the full maneuver horizon, and the predicted value of the current state is set to infinity.
    GuidanceFlag $\leftarrow$ true; $\boldsymbol{t}_k \leftarrow \boldsymbol{t}$; $\boldsymbol{y}_{\text{pred}} \leftarrow \infty$;
  else
    $t_{k-1} \leftarrow$ Element with index $(k-1)$ in $\boldsymbol{t}$; // Previous step
    $\tilde{\boldsymbol{x}}_{c,k}$, $\tilde{\boldsymbol{\alpha}}_{c,k} \leftarrow$ Propagate chief's orbit $t_{k-1} \to t_k$; // Propagation from the previous to the current step
    if k *is even*, **then** // A step at which the thruster is turned on
      GuidanceFlag $\leftarrow$ true; // A new guidance profile will be calculated.
      $\boldsymbol{t}_k \leftarrow$ Elements $(k+2) \to$ **last** in $\boldsymbol{t}$; // The current horizon spans from current to the final step.
      $\boldsymbol{y}_{\text{pred}} \leftarrow$ Column 2 in $\boldsymbol{Y}_k$; // A prediction of the current state is extracted from previous guidance.
      $\tilde{\boldsymbol{x}}_{d,k}$, $\tilde{\boldsymbol{\alpha}}_{d,k} \leftarrow$ Propagate deputy $t_{k-1} \to t_k$; // Propagation from previous step to current step
    else
      GuidanceFlag $\leftarrow$ false; // No need to calculate a new guidance profile
  $\boldsymbol{\alpha}_{c,k} \leftarrow$ Osc2Mean$(\tilde{\boldsymbol{\alpha}}_{c,k})$; // Transforming osculating elements of the chief into mean ones
  if GuidanceFlag, **then**
    $\boldsymbol{\alpha}_{d,k} \leftarrow$ Osc2Mean$(\tilde{\boldsymbol{\alpha}}_{d,k})$; // Transforming osculating elements of the deputy into mean ones
    $\check{\boldsymbol{x}}_{c,k}$, $\check{\boldsymbol{\alpha}}_{c,k} \leftarrow$ Apply Eq . (15) on $\boldsymbol{\alpha}_{c,k}$; // Adding disturbances the the chief's states
    $\check{\boldsymbol{y}}_k \leftarrow$ Apply Eq . (17) on $\boldsymbol{\alpha}_{c,k}$ and $\boldsymbol{\alpha}_{d,k}$; // Adding disturbances to the dimensional ROE vector
    if $\|\check{\boldsymbol{y}}_k - \boldsymbol{y}_{\text{pred}}\| \geq \epsilon$, **then** // The current state is not close to the predicted one
      $\boldsymbol{Y}_k$, $\boldsymbol{F}_k \leftarrow$ Solve Problem 2 using $\boldsymbol{t}_k$, $\check{\boldsymbol{y}}_k$, $\boldsymbol{y}_f$; // Solving for a new guidance profile
      if Solver did not succeed, **then**
        if $k = 0$, **then** // Problem is infeasible for the given $\boldsymbol{t}$ vector.
          break;
        NoUpdateFlag $\leftarrow$ true; // When the current guidance fails, the previous guidance profile is kept.
    else
      NoUpdateFlag $\leftarrow$ true; // When the current state is close to the predicted one, old guidance is kept.
    if NoUpdateFlag, **then** // Sticking to the previous guidance profile
      $\boldsymbol{Y}_k \leftarrow$ Columns $2 \to$ **last** in $\boldsymbol{Y}_{k-2}$; // Aligning the previous guidance with the current horizon
      $\boldsymbol{F}_k \leftarrow$ Columns $2 \to$ **last** in $\boldsymbol{F}_{k-2}$;
    $\boldsymbol{f}^r_{k|k+1} \leftarrow$ Column 0 in $\boldsymbol{F}_k$, divided by $\frac{a_c}{M}$; // Refer to Eq. (5).
  else // Guidance is not solved because the current step is the start of a thruster-off period.
    $\boldsymbol{f}^r_{k|k+1} \leftarrow \boldsymbol{0}$;
  $\check{\boldsymbol{f}}^r_{k|k+1} \leftarrow$ Apply Eq. (19) and saturation on $\boldsymbol{f}^r_{k|k+1}$; // Adding the effect of pointing error to thrust vector
  $\check{\boldsymbol{f}}^i_{k|k+1} \leftarrow$ Rotate $\check{\boldsymbol{f}}^r_{k|k+1}$ from $\mathbb{F}^r$ to $\mathbb{F}^i$ using $\check{\boldsymbol{x}}_{c,k}$.
  $\tilde{\boldsymbol{x}}_{d,k+1}$, $\tilde{\boldsymbol{\alpha}}_{d,k+1} \leftarrow$ Propagate deputy $t_k \to t_{k+1}$ with constant thrust $\check{\boldsymbol{f}}^i_{k|k+1}$.

Table 3 Benchmark simulation parameters

Parameter	Value	Parameter	Value
$t_f - t_0$, orbits	7	$\sigma_{\boldsymbol{r}_d} \equiv \sigma_{\boldsymbol{r}_c}$, m	10
$\sigma_{\boldsymbol{v}_d} \equiv \sigma_{\boldsymbol{v}_c}$, m/s	0.5	$\sigma_{\boldsymbol{y}}$, m/s	1
ζ_{pe}, arcs	25	ϵ, m	5

that the guidance is skipped and the previous guidance profile is used. It is important to note that the elapsed time in Fig. 11 corresponds to the time it takes to construct and solve the problem using the OSQP solver [25] interfaced with MATLAB® and run on an eight-core Intel Core i9-10885H processor. It is clear from Fig. 11 that the elapsed time for every guidance run is getting smaller as the simulation advances because the size of the problem is getting

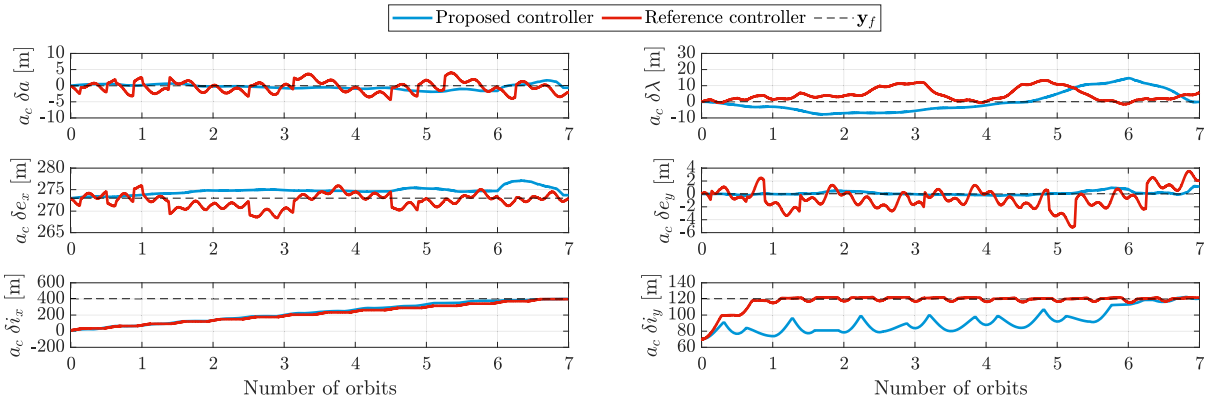

Fig. 9 Closed-loop dimensional ROE profile.

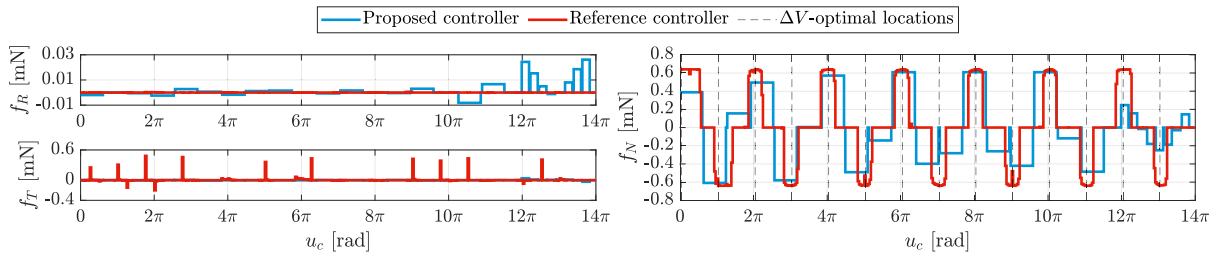

Fig. 10 Closed-loop thrust profile in the RTN frame.

Table 4 Comparison between the proposed and the reference MPCs

MPC strategy	Terminal $\boldsymbol{y}$ error, m	ΔV_{tot}, m/s
Proposed	$[-0.6 \quad -0.1 \quad 0.7 \quad 1.1 \quad -0.3 \quad 0.3]^{\intercal}$	0.65
Reference	$[3.6 \quad -9.2 \quad 1.4 \quad -2.0 \quad 2.9 \quad -1.6]^{\intercal}$	0.5

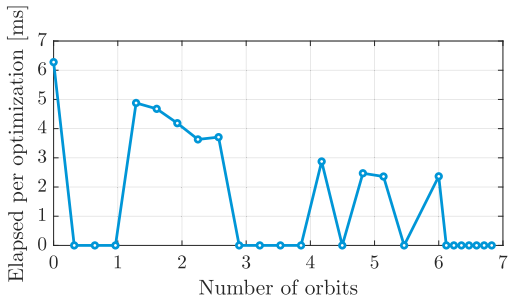

Fig. 11 Elapsed time to solve problem 2.

smaller as the guidance problem is always solved from the current to the final time.

VI. Conclusions

This Note proposes a novel approach for guidance of an underactuated spacecraft to perform relative orbit corrections with respect to a reference satellite. The guidance scheme not only considers the typical constraints of the main spacecraft while performing the maneuver, but it also considers the dynamical constraint which arises from the satellite being equipped with a single electric thruster. Thanks to parameterizing the relative dynamics between the two spacecraft using the quasi-nonsingular relative orbital elements, the guidance problem was formulated as a quadratic programming problem, which, if feasible, is guaranteed to have exactly one solution that can be found using high-performance standard quadratic programming solvers. The proposed guidance scheme shows numerous inherent merits which include fuel optimality and the ability to support long no-thrust periods arising from operational constraints. The Note also proposes a model-predictive-control scheme to close the control loop, which does not require the guidance optimization to run at the beginning of each prediction horizon. This closed-loop system has been validated via high-fidelity numerical simulations in which navigation and actuators' errors and constraints are emulated, and its performance is benchmarked against that of a reference controller from the literature. The proposed guidance and control algorithms have shown superior performance over the reference controller for the benchmark simulation in terms of terminal tracking errors.

Acknowledgments

This research was funded in whole, or in part, by the Luxembourg National Research Fund, grant reference BRIDGES/19/MS/1430 2465. For the purpose of open access, and in fulfilment of the obligations arising from the grant agreement, the author has applied a Creative Commons Attribution 4.0 International (CC BY 4.0) license to any Author Accepted Manuscript version arising from this submission.

References

[1] Miller, S., Walker, M. L. R., Agolli, J., and Dankanich, J., "Survey and Performance Evaluation of Small-Satellite Propulsion Technologies," *Journal of Spacecraft and Rockets*, Vol. 58, No. 1, 2021, pp. 222–231. https://doi.org/10.2514/1.A34774

[2] Krejci, D., and Lozano, P., "Space Propulsion Technology for Small Spacecraft," *Proceedings of the IEEE*, Vol. 106, No. 3, 2018, pp. 362–378. https://doi.org/10.1109/JPROC.2017.2778747

[3] Helmeid, E., Buursink, J., Poppe, M., Ries, P., and Gales, M., "The Integrated Avionics Unit - Performance, Innovation and Application," *4S Symposium, 2022*, ESA-ESTEC, Noordwijk, The Netherlands, ESA Conference Bureau, 2022, https://az659834.vo.msecnd.net/eventsairwesteuprod/production-atpi-public/7d45491b26234d388fa52afdbc19814b.

[4] Stanzione, V., and Sabbatinelli, B., "PLATiNO Project: A New Italian Multi-Application Small Satellite Platform for Highly Competitive Missions," *69th International Astronautical Congress (IAC)*, International Astronautical Federation, Bremen, Germany, 2018, https://dl.iafastro.directory/event/IAC-2018/paper/47097/.

[5] Floberghagen, R., Fehringer, M., Lamarre, D., Muzi, D., Frommknecht, B., Steiger, C., Piñeiro, J., and da Costa, A., "Mission Design, Operation and Exploitation of the Gravity Field and Steady-State Ocean Circulation Explorer Mission," *Journal of Geodesy*, Vol. 85, No. 11, 2011, pp. 749–758. https://doi.org/10.1007/s00190-011-0498-3

[6] Larsson, R., Noteborn, R., Bodin, P., Simone, D., Karlsson, T., and Carlsson, A., "Autonomous Formation Flying in LEO - Seven Months of Routine Formation Flying with Frequent Reconfigurations," *4th International Conference on Spacecraft Formation Flying Missions & Technologies*, Canadian Space Agency (CSA), Saint-Hubert, QC, Canada, 2011, https://elib.dlr.de/74364/.

[7] Gaias, G., and D'Amico, S., "Impulsive Maneuvers for Formation Reconfiguration Using Relative Orbital Elements," *Journal of Guidance, Control, and Dynamics*, Vol. 38, No. 6, 2015, pp. 1036–1049. https://doi.org/10.2514/1.G000189

[8] Di Mauro, G., Bevilacqua, R., Spiller, D., Sullivan, J., and D'Amico, S., "Continuous Maneuvers for Spacecraft Formation Flying Reconfiguration Using Relative Orbit Elements," *Acta Astronautica*, Vol. 153, Dec. 2018, pp. 311–326. https://doi.org/10.1016/j.actaastro.2018.01.043

[9] Chernick, M., and D'Amico, S., "New Closed-Form Solutions for Optimal Impulsive Control of Spacecraft Relative Motion," *Journal of Guidance, Control, and Dynamics*, Vol. 41, No. 2, 2018, pp. 301–319. https://doi.org/10.2514/1.G002848

[10] Scala, F., Gaias, G., Colombo, C., and Martín-Neira, M., "Design of Optimal Low-Thrust Manoeuvres for Remote Sensing Multi-Satellite Formation Flying in Low Earth Orbit," *Advances in Space Research*, Vol. 68, No. 11, 2021, pp. 4359–4378. https://doi.org/10.1016/j.asr.2021.09.030

[11] De Vittori, A., Palermo, M. F., Lizia, P. D., and Armellin, R., "Low-Thrust Collision Avoidance Maneuver Optimization," *Journal of Guidance, Control, and Dynamics*, Vol. 45, No. 10, 2022, pp. 1815–1829. https://doi.org/10.2514/1.G006630

[12] Gaias, G., and Ardaens, J.-S., "Flight Demonstration of Autonomous Noncooperative Rendezvous in Low Earth Orbit," *Journal of Guidance, Control, and Dynamics*, Vol. 41, No. 6, 2018, pp. 1337–1354. https://doi.org/10.2514/1.G003239

[13] Gaias, G., D'Amico, S., and Ardaens, J.-S., "Generalised Multi-Impulsive Manoeuvres for Optimum Spacecraft Rendezvous in

Near-Circular Orbit," *International Journal of Space Science and Engineering*, Vol. 3, No. 1, 2015, pp. 68–88.
https://doi.org/10.1504/IJSPACESE.2015.069361

[14] Belloni, E., Silvestrini, S., Prinetto, J., and Lavagna, M., "Relative and Absolute On-Board Optimal Formation Acquisition and Keeping for Scientific Activities in High-Drag Low-Orbit Environment," *Recent Advances in Satellite Constellations and Formation Flying, Advances in Space Research*, Vol. 73, No. 11, 2024, pp. 5595–5613.
https://doi.org/10.1016/j.asr.2023.07.051

[15] Mahfouz, A., Gaias, G., Venkateswara, D. M. K. K., and Voos, H., "Autonomous Optimal Absolute Orbit Keeping Through Formation-Flying Techniques," *Aerospace*, Vol. 10, No. 11, 2023.
https://doi.org/10.3390/aerospace10110959

[16] Menzio, D., Mahfouz, A., Vedova, D., et al., "Formation Design of an Inter-Satellite Link Demonstration Mission," *Proceedings of the 11th International Workshop on Satellite Constellations & Formation Flying*, International Astronautical Federation (IAF), Paris, France, 2022, Paper 62, https://hdl.handle.net/10993/53602.

[17] Mahfouz, A., Mezio, D., Dalla-Vedova, F., and Voos, H., "Relative State Estimation for LEO Formations with Large Inter-Satellite Distances Using Single-Frequency GNSS Receivers," *Proceedings of the 11th International Workshop on Satellite Constellations & Formation Flying*, International Astronautical Federation (IAF), Paris, France, 2022, Paper 15, https://hdl.handle.net/10993/53601.

[18] Mahfouz, A., Mezio, D., Dalla-Vedova, F., and Voos, H., "GNSS-Based Baseline Vector Determination for Widely Separated Cooperative Satellites Using L1-Only Receivers," *Advances in Space Research*, Vol. 73, No. 11, 2023, pp. 5570–5581.
https://doi.org/ 10.1016/j.asr.2023.06.037

[19] Morgan, D., Chung, S.-J., and Hadaegh, F. Y., "Model Predictive Control of Swarms of Spacecraft Using Sequential Convex Programming," *Journal of Guidance, Control, and Dynamics*, Vol. 37, No. 6, 2014, pp. 1725–1740.
https://doi.org/10.2514/1.G000218

[20] Ross, I. M., "Space Trajectory Optimization and L1-Optimal Control Problems," *Modern Astrodynamics, Elsevier Astrodynamics Series*, edited by P. Gurfil, Vol. 1, Butterworths, London, 2006, Chap. 6.
https://doi.org/10.1016/S1874-9305(07)80008-2

[21] Vallado, D. A., *Fundamentals of Astrodynamics and Applications*, 4th ed., Microcosm Press & Springer, Hawthorne, CA, 2013, pp. 95–105, Chap. 2.

[22] Gaias, G., Colombo, C., and Lara, M., "Analytical Framework for Precise Relative Motion in Low Earth Orbits," *Journal of Guidance, Control, and Dynamics*, Vol. 43, No. 5, 2020, pp. 915–927.
https://doi.org/10.2514/1.G004716

[23] Boyd, S. P., and Vandenberghe, L., *Convex Optimization*, Vol. 4, Cambridge Univ. Press, Cambridge, England, U.K., 2004, pp. 136–137.

[24] Camino, J.-T., Artigues, C., Houssin, L., and Mourgues, S., "Linearization of Euclidean Norm Dependent Inequalities Applied to Multibeam Satellites Design," *Computational Optimization and Applications*, Vol. 73, No. 2, 2019, pp. 679–705.
https://doi.org/10.1007/s10589-019-00083-z

[25] Stellato, B., Banjac, G., Goulart, P., Bemporad, A., and Boyd, S., "OSQP: An Operator Splitting Solver for Quadratic Programs," *Mathematical Programming Computation*, Vol. 12, No. 4, 2020, pp. 637–672.
https://doi.org/10.1007/s12532-020-00179-2

[26] D'Amico, S., Ardaens, J.-S., and Montenbruck, O., "Navigation of Formation Flying Spacecraft Using GPS: The PRISMA Technology Demonstration," *Proceedings of the 22nd International Technical Meeting of the Satellite Division of The Institute of Navigation (ION GNSS 2009)*, The Inst. of Navigation, Manassas, VA, 2009, pp. 1427–1441, https://www.ion.org/publications/abstract.cfm?articleID=8552.

S. D'Amico
Associate Editor